Compact-Reconstruction Weighted Essentially Non-Oscillatory Schemes for the Unsteady Navier-Stokes Equations

Debojyoti Ghosh,[*] Shivaji Medida[†] and James D. Baeder[‡]

University of Maryland, College Park, MD, 20742

Non-linear compact interpolation schemes, based on the Weighted Essentially Non-Oscillatory algorithm, are applied to the unsteady Navier-Stokes equations in this paper. The schemes have been demonstrated to have superior accuracy and spectral properties compared to non-compact schemes of the same order of convergence. Their performance has been assessed for scalar conservation laws and the inviscid Euler equations on equally spaced meshes and it was observed that the compact schemes show sharper resolution of discontinuities and high-frequency waves as well as lower absolute errors. This paper presents the application of these schemes to viscous, turbulent flows on body-fitted meshes. The compact reconstruction scheme is incorporated into a high-order accurate Navier-Stokes flow solver and its performance is verified for practical flow problems on domains involving overset and moving mesh systems.

I.   Introduction

The Navier-Stokes equations govern the dynamics of a fluid satisfying the continuum assumption.[1] They can be simplified to the Euler equations[2] by assuming zero viscosity and thermal conductivity. The Euler equations can be used to model the flow of high Reynolds number flows where viscous effects are negligible. The convective terms in these systems of equations are hyperbolic in nature and thus, the solution is composed of waves traveling at their characteristic speeds. While the Euler equations admit discontinuous solutions, solutions to the Navier-Stokes equations may have steep gradients due to viscous shock waves and thin boundary layers. High order numerical schemes based on polynomial interpolation need solution-dependent limiting to ensure non-oscillatory solutions. Several such methods have been proposed[2] and applied to the Euler and Navier-Stokes equations.

The Essentially Non-Oscillatory (ENO) schemes were introduced[3] which use adaptive stenciling to achieve non-oscillatory interpolation. At each point where the interpolated solution is desired, the ENO schemes use the "smoothest" stencil amongst candidate stencils of the desired order. The "smoothness" of a stencil is measured by the divided differences. The ENO schemes were further developed into finite difference forms and extended to systems of equations.[4,5] The Weighted Essentially Non-Oscillatory (WENO) schemes were introduced[6] where a convex combination of candidate stencils are used. A weighted combination of r-th order candidate stencils is used with weights that are based on the smoothness of the stencil. At smooth regions of the solution, the weights attain their optimal values such that the combination is a higher order interpolation scheme. At discontinuities, the weights for the stencils containing the discontinuity approach zero, resulting in a non-oscillatory interpolation. An improved WENO scheme was presented[7] where the improved smoothness indicators allowed the construction of a $(2r - 1)$-th order WENO scheme from the underlying r-th order ENO scheme. Third and fifth order WENO schemes ($r = 2, 3$) were constructed with these smoothness indicators and extended to higher orders ($r = 4, 5, 6$).[8] The WENO schemes presented in[7] were seen to be sensitive to the value of an arbitrary parameter and did not converge at the optimal order

---

[*]Graduate Student, Applied Mathematics & Statistics, and Scientific Computation, ghosh@umd.edu, and AIAA Student Member.

[†]Graduate Student, Aerospace Engineering, smedida@umd.edu, and AIAA Student Member.

[‡]Associate Professor, Aerospace Engineering, baeder@umd.edu, and AIAA Associate Fellow.

for certain cases of smooth solutions. A mapping of the weights was proposed[9] where the weights converged much faster to their optimal values.

Compact schemes were introduced[12] which achieve high orders of accuracy with smaller stencils. Compact schemes have better spectral properties resulting in the improved resolution of high frequency waves compared to non-compact schemes. The application of compact schemes to hyperbolic partial differential equations requires the enforcement of a limiter to ensure non-oscillatory behavior across discontinuities. Several efforts have been made to combine the WENO schemes with compact schemes to achieve high-resolution, non-oscillatory schemes that are capable of resolving a large range of length scales seen in compressible, turbulent flows. One such family of schemes are the hybrid Compact-WENO schemes[13,14] where a compact scheme is used to compute the solution at smooth regions of the flow and the WENO scheme is used at and near discontinuities. A smoothness indicator is used to switch between the two schemes. While this results in a non-oscillatory scheme, a non-compact scheme is used to compute the solution around discontinuities and thus, the improved spectral properties of the compact scheme are lost due to this coupling. An alternative family of schemes[15–17] used the ENO or WENO schemes to compute a high-order accurate approximation of the interface flux. The first derivative of the flux at the cell-centers was computed using high-order compact schemes from the interface fluxes. The resulting scheme showed only a marginal improvement in the spectral resolution since the interface fluxes were computed using a non-compact interpolation.

A new class of non-linear compact schemes were introduced by the authors[18] based on the WENO algorithm of adaptive stenciling. Lower order compact interpolation stencils were identified at each interface and optimal weights were calculated such that the weighted combination would result in a higher-order compact interpolation scheme. The WENO weights are computed based on the smoothness of the stencil such that they approach the optimal weights for smooth solutions and approach zero for stencils containing discontinuities. The resulting scheme is thus a high-order accurate compact scheme for smooth solutions and a low-order accurate biased compact scheme at discontinuities. The performance of the resulting Compact-Reconstruction WENO (CRWENO) schemes was analyzed for the scalar conservation law for smooth as well as discontinuous solutions. It was observed that the CRWENO schemes showed a significantly lower absolute error for the same order of convergence. The CRWENO schemes showed reduced smearing of discontinuities and clipping of extrema, especially for long-term convection. The CRWENO schemes were applied to the one- and two-dimensional Euler equations on equally spaced grids. The new schemes showed lower absolute errors for the same order of convergence, compared to the WENO schemes. The improved spectral resolution and the lower dissipation resulted in the improved preservation of vortical structures and sharper resolution of high-frequency waves, while yielding non-oscillatory solutions across discontinuities.

The application of the CRWENO scheme to the unsteady Navier-Stokes equations is presented in this paper. Benchmark flow cases for the inviscid Euler equations are presented that demonstrate the improved numerical properties of the scheme. The sound generation from the interaction of a vortex with a shock wave is presented as a verification of the algorithm's ability to accurately capture acoustic waves. The steady, viscous flow around the RAE2822 airfoil is simulated to assess the performance of the CRWENO scheme on a curvilinear mesh and the results are validated with experimental data.[30] The dynamic stall of the SC1095 airfoil in a wind tunnel[33] is studied as the domain requires an overset mesh system with relative motion between the airfoil and wind tunnel grids. Finally, the turbulent flow around a pitching-plunging NACA0005 at low Reynolds number is simulated. This case is representative of flow around a flapping-wing-based micro-air vehicle and our results are compared with previous computational studies.[34] The pitching and plunging motion of the airfoil results in the creation and shedding of vortices from the upper surface. Integrated quantities like lift and drag are verified and show good agreement with previous results. However, the high resolution compact scheme, along with a delayed detached eddy turbulence model, is able to capture the smaller length scales of the flow near the airfoil surface as well as acoustic waves generated by the interaction of shed vortices and the airfoil.

II.   Governing Equations

The compressible Navier-Stokes equations[1] govern the behavior of a Newtonian fluid. The conservation of mass for a differential fluid element can be expressed as

$$\frac{\partial \rho}{\partial t} + \frac{\partial (\rho u_i)}{\partial x_i} = 0 \tag{1}$$

The momentum conservation equations are

$$\frac{\partial(\rho u_i)}{\partial t} + \frac{\partial(\rho u_i u_j)}{\partial x_j} = -\frac{\partial p}{\partial x_i} + \frac{\partial \tau_{ij}}{\partial x_j} \tag{2}$$

and the equation for energy conservation is

$$\frac{\partial e}{\partial t} + \frac{\partial u_i(e+p)}{\partial x_i} = \frac{\partial(u_j \tau_{ij})}{\partial x_i} + k \sum_i \frac{\partial T}{\partial x_i} \tag{3}$$

where i, j are indices for the spatial dimensions, ρ is the density of the fluid, u_i is the component of the velocity vector along x_i, p is the static pressure, e is the internal energy and T is the static temperature. The coefficient of thermal conductivity is k and the equation of state relates the internal energy to the pressure and velocity as

$$e = \frac{p}{\gamma - 1} + \frac{1}{2}\rho u_i u_i \tag{4}$$

where γ is the ratio of specific heats. The temperature is related to the pressure and density as $p = \rho R T$ for a perfect gas where R is the universal gas constant. The viscous stresses are given by

$$\tau_{ij} = \mu[(\frac{\partial u_i}{\partial x_j} + \frac{\partial u_j}{\partial x_i}) - \frac{2}{3}\frac{\partial u_k}{\partial x_k}\delta_{ij}] \tag{5}$$

where μ is the laminar viscosity coefficient. The inviscid Euler equations can be obtained from the Navier-Stokes equations by setting the viscous and thermal conductivity terms to zero.

III.   Numerical Method

The Navier-Stokes equations form a hyperbolic-parabolic system of partial differential equations (PDE) where the convective fluxes are hyperbolic in nature while the viscous terms are parabolic. Equations 1-3 can be expressed in the vector form as

$$\frac{\partial \mathbf{Q}}{\partial t} + \frac{\partial \mathbf{F}_i}{\partial x_i} = \frac{\partial \mathbf{F}_i^v}{\partial x_i} \tag{6}$$

where $\mathbf{Q} = [\rho \ \rho \mathbf{u} \ \mathbf{e}]^{\mathbf{T}}$ is the vector of conserved quantities and $\mathbf{F}, \mathbf{F^v}$ are the convective and viscous fluxes respectively. The system is discretized in space to yield an ordinary differential equation in time. Considering the one-dimensional system, a conservative finite difference discretization of the convective flux terms results in

$$\frac{\partial \mathbf{Q}_j}{\partial t} + \frac{1}{\Delta x}[\mathbf{H}(x_{j+1/2}) - \mathbf{H}(x_{j-1/2})] = \frac{1}{\Delta x}\delta \mathbf{F}^v(x_j) \tag{7}$$

where j is the grid index and $\mathbf{Q}_j$ is the cell-centered value of $\mathbf{Q}$. The numerical approximation to the viscous terms at the j-th cell is given by $\delta \mathbf{F}^v(x_j)$ and $\mathbf{H}$ is the numerical flux function which is required to exactly satisfy[9]

$$\frac{\partial \mathbf{F}}{\partial x}\bigg|_{x=x_j} = \frac{1}{\Delta x}[\mathbf{H}(x_{j+1/2}) - \mathbf{H}(x_{j-1/2})] \tag{8}$$

The reconstruction step, outlined in the next section, involves the approximation (at the desired order) of the numerical flux at the cell interfaces $(x_{j+1/2})$ from the discrete cell-centered values of the flux $(\mathbf{F}(x_j))$. The viscous terms are discretized using second order central differencing. In our current study, Eq. 7 is marched in time using the explicit third order Total Variation Diminishing Runge-Kutta (TVDRK3) scheme or the implicit second order Backward Difference Formula (BDF2) with Newton sub-iterations for time accuracy.[19] The linear system resulting from the implicit time marching is solved iteratively using the Lower-Upper Symmetric Gauss-Seidel (LUSGS) scheme[20,21] or the diagonalized ADI scheme.[22,23] The governing equations are modified using the Low Mach Preconditioning Method[24] to accelerate the convergence and prevent oscillatory solutions for low Mach incompressible flows. The Spalart-Allmaras model[25] is used for cases where the flow is turbulent.

IV.   Reconstruction

The reconstruction step involves the approximation of the interface fluxes $\mathbf{H}(x_{j+1/2})$ from the discrete cell-centered fluxes $\mathbf{F}(x_j)$ at the desired order. A biased interpolation is required ("upwinding") to respect the wave nature of the solution to hyperbolic PDEs. In the present section, the left-biased reconstruction of a scalar quantity using the CRWENO scheme is described and then extended to a vector flux (for the Navier-Stokes equations). Considering Eq. 8 for a scalar flux function $f(x)$, the reconstruction of the numerical flux function $h(x)$ is required at the cell interfaces. An approximate flux function $\hat{f}(x) \approx h(x)$ is computed from the discrete values of the flux function $f(x_j)$ such that

$$
\begin{aligned}
\left.\frac{\partial f}{\partial x}\right|_{x=x_j} &= \frac{h_{j+1/2} - h_{j-1/2}}{\Delta x} \\
&= \frac{\hat{f}_{j+1/2} - \hat{f}_{j-1/2}}{\Delta x} + O(\Delta x^r)
\end{aligned}
\tag{9}
$$

where r is the desired order of the scheme. Hyperbolic PDEs admit discontinuous solutions and thus, a high order polynomial interpolation would result in spurious oscillations. The WENO schemes use adaptive stenciling to yield non-oscillatory (lower order accurate) solution near or across discontinuities while achieving high order accuracy in smooth regions of the flow. This algorithm is applied to compact interpolation stencils to yield the CRWENO scheme.

At a given interface $x_{j+1/2}$, an r-th order interpolation has r candidate stencils which contain the j-th grid cell. The WENO schemes[6,7] use a combination of these r-order candidate stencils at an interface to get a higher order interpolation in smooth regions and a non-oscillatory interpolation near discontinuities. The general form of the interface flux is

$$
\hat{f}_{j+1/2} = \sum_{k=1}^{r} \omega_k \hat{f}_{j+1/2}^k
\tag{10}
$$

where $f_{j+1/2}^k$ is the interpolated flux at $x_{j+1/2}$ using the k-th candidate stencil and ω_k is the weight of k-th stencil. Optimal weights c_k, $k = 1, \ldots, r$ exist such that $\omega_k = c_k \forall k$ yields a $(2r - 1)$-th order accurate interpolation. However, across or near discontinuities, use of the optimal weights would result in an oscillatory interpolation (from stencils that contain the discontinuity). Thus, the WENO weight of each stencil is computed by scaling the optimal weight by the "smoothness" of that stencil, i.e.,

$$
\alpha_k = \frac{c_k}{(\beta_k + \epsilon)^m}
\tag{11}
$$

where β_k is the smoothness indicator of the k-th stencil and ϵ is a small number to prevent division by zero. The exponent m is chosen such that the weights for non-smooth stencils approach zero quickly (in the present study, $m = 2$ is used for all cases). The weights α_k are normalized as

$$
\omega_k = \frac{\alpha_k}{\sum_k \alpha_k}
\tag{12}
$$

to ensure convexity.

The weights, defined by Jiang and Shu, have been shown to be excessively dissipative and non-optimal convergence was observed for certain types of smooth solutions. Several modifications to the weights have been proposed in literature. A mapping of the weights has been proposed[9] that causes the WENO weights to converge faster to their optimal values, however, the mapping function adds to the computation cost. Different formulations for the weights have been presented[10,11] which reduce the dissipation and improve the convergence properties of the WENO schemes.

High order WENO schemes using non-compact interpolation require wide stencils that may lead to loss of accuracy and oscillatory solutions. In addition, they suffer from poor spectral properties. Thus, the Compact-Reconstruction WENO schemes were proposed[18] where the candidate stencils are compact with implicit interpolation. There are r candidate compact stencils at an interface for a r-th order interpolation. Optimal weights exist for each stencil such that their combination yields a $(2r - 1)$-th order compact interpolation. Thus, the CRWENO scheme applies the WENO algorithm, given by Eqs. 10-12, to the compact interpolation stencils. The resulting scheme has lower absolute errors and smaller stencils for the same order of convergence, as well as higher spectral resolution.
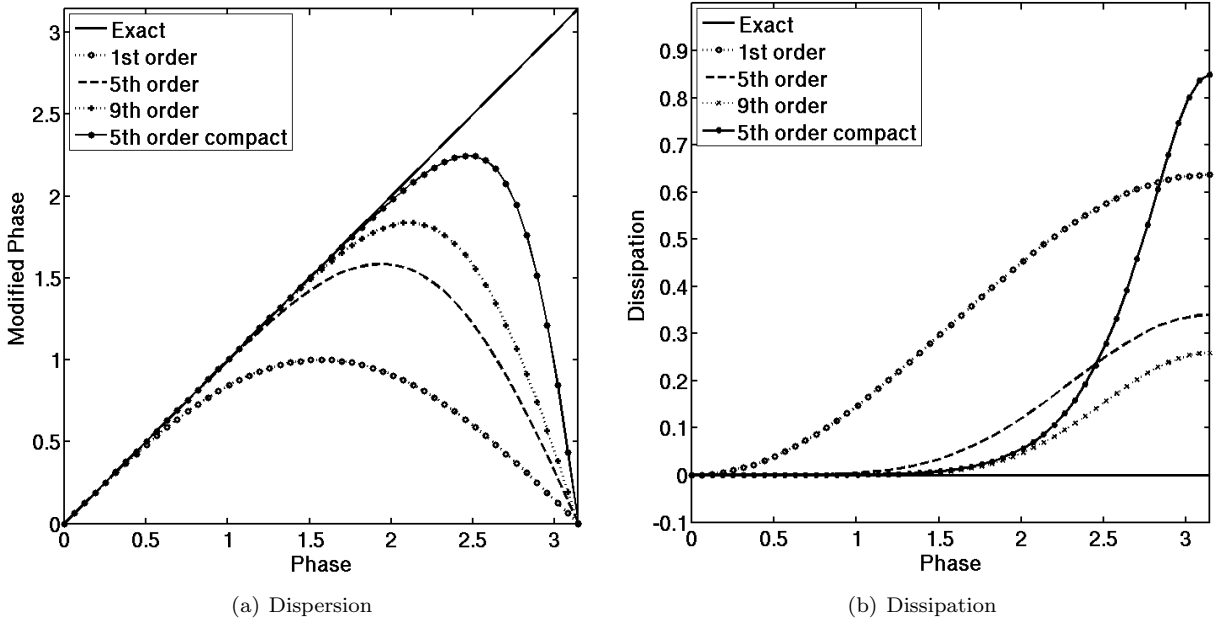
American Institute of Aeronautics and Astronautics

(a) Dispersion   (b) Dissipation

Figure 1. Spectral characteristics of the first order, non-compact 5th order, non-compact 9th order and compact 5th order schemes

The fifth order CRWENO scheme (CRWENO5) is described. The three third order compact interpolations at $x_{j+1/2}$ are

$$\frac{2}{3}\hat{f}^1_{j-1/2} + \frac{1}{3}\hat{f}^1_{j+1/2} = \frac{1}{6}(f_{j-1} + 5f_j) \tag{13}$$

$$\frac{1}{3}\hat{f}^2_{j-1/2} + \frac{2}{3}\hat{f}^2_{j+1/2} = \frac{1}{6}(5f_j + f_{j+1}) \tag{14}$$

$$\frac{2}{3}\hat{f}^3_{j+1/2} + \frac{1}{3}\hat{f}^3_{j+3/2} = \frac{1}{6}(f_j + 5f_{j+1}) \tag{15}$$

with optimal weights as $c_1 = 1/5, c_2 = 1/2, c_3 = 3/10$. The optimal fifth order compact interpolation scheme, which is the weighted combination of the three third order interpolations, is

$$\frac{3}{10}\hat{f}_{j-1/2} + \frac{6}{10}\hat{f}_{j+1/2} + \frac{1}{10}\hat{f}_{j+3/2} = \frac{1}{30}f_{j-1} + \frac{19}{30}f_j + \frac{10}{30}f_{j+1} \tag{16}$$

Figure 1 shows the spectral properties of the compact scheme given by Eq. 16. The fifth order compact scheme shows a significantly higher resolution than the fifth and ninth non-compact schemes (which are the optimal equivalents of the fifth order and ninth order WENO schemes) and is able to accurately capture higher frequencies on the same grid. The dissipation for the fifth order compact scheme is lower than the fifth order non-compact scheme and comparable to the ninth order non-compact scheme for lower and mid-range frequencies. At higher frequencies, where aliasing errors are large, the higher dissipation of the compact scheme filters out the high-frequency errors.

The WENO weights are computed using the smoothness indicators that are given by

$$\beta_1 = \frac{13}{12}(f_{j-2} - 2f_{j-1} + f_j)^2 + \frac{1}{4}(f_{j-2} - 4f_{j-1} + 3f_j)^2 \tag{17}$$

$$\beta_2 = \frac{13}{12}(f_{j-1} - 2f_j + f_{j+1})^2 + \frac{1}{4}(f_{j-1} - f_{j+1})^2 \tag{18}$$

$$\beta_3 = \frac{13}{12}(f_j - 2f_{j+1} + f_{j+2})^2 + \frac{1}{4}(3f_j - 4f_{j+1} + f_{j+2})^2 \tag{19}$$

and the weights can thus be computed using Eqs. 11 and 12. The resulting scheme is given by

$$(\frac{2}{3}\omega_1 + \frac{1}{3}\omega_2)\hat{f}_{j-1/2} + (\frac{1}{3}\omega_1 + \frac{2}{3}(\omega_2 + \omega_3))\hat{f}_{j+1/2} + \frac{1}{3}\omega_3\hat{f}_{j+3/2}$$

$$= \frac{\omega_1}{6}f_{j-1} + \frac{5(\omega_1 + \omega_2) + \omega_3}{6}f_j + \frac{\omega_2 + 5\omega_3}{6}f_{j+1} \tag{20}$$

American Institute of Aeronautics and Astronautics

The system of equations represented by Eqs. 20 is tridiagonal and the convexity of weights ensures non-zero terms on the main diagonal.

Although the Compact-Reconstruction WENO schemes require the solution of a system of equations, the sparse nature of the system results in a computational cost of $O(N)$ where N is the grid size. It is, therefore, of the same order as the traditional WENO schemes. Compact interpolations result in a significantly lower absolute error at the same grid resolution thus justifying the additional computational expense.

IV.A. Extension to the Navier-Stokes Equations

The previous sub-sections describe the application of the CRWENO scheme to a scalar quantity. The numerical solution of the Navier-Stokes equations requires the reconstruction of a vector quantity at the interfaces. The scalar interpolation techniques can be extended to the system of equations in three possible ways - interpolation of the primitive, conserved or the characteristic variables. The first approach interpolates the primitive flow variables (ρ, $\mathbf{u}$, p) at each interface from their cell-centered values. Similarly, the second approach interpolates the conserved quantities (ρ, $\rho\mathbf{u}$, e) from their cell-centered values. Thus it can be seen as applying the scalar reconstruction process separately on each equation of the system. The reconstruction schemes of the previous sub-sections can be trivially extended to a system of equation for these two approaches.

The hyperbolic nature of the convective fluxes implies that the solution is composed of waves propagating at their characteristic speeds (given by the eigenvalues of the flux Jacobian) along their characteristic paths. The computation of interface fluxes needs to model this wave behavior by the process of upwinding. For the one-dimensional system, left and right biased interface fluxes ($\hat{\mathbf{F}}^L_{j+1/2}, \hat{\mathbf{F}}^R_{j+1/2}$,) are computed at the interface, where $\hat{\mathbf{F}}_{j+1/2}$ is an approximation of the numerical flux function $\mathbf{H}(x_{j+1/2})$. The previous sub-sections describe left-biased interpolations where the flux at the interface $x_{+1/2}$ is computed using a stencil centered on the j-th cell. A right-biased interpolation can be obtained by reflecting the equations across the interface where the stencil is centered on the $(j+1)$-th cell. The Roe flux differencing[26] is used in the current algorithm to find the upwind interface flux, which is given by

$$\hat{\mathbf{F}}_{j+1/2} = \frac{1}{2}(\hat{\mathbf{F}}^L_{j+1/2} + \hat{\mathbf{F}}^R_{j+1/2}) - \frac{1}{2}|\hat{A}(\hat{\mathbf{Q}}^L_{j+1/2}, \hat{\mathbf{Q}}^R_{j+1/2})|(\hat{\mathbf{Q}}^L_{j+1/2} + \hat{\mathbf{Q}}^R_{j+1/2}) \tag{21}$$

where $\hat{A}$ is the Roe-averaged Jacobian matrix. $\hat{\mathbf{Q}}^{L,R}_{j+1/2}$ are the left and right biased reconstructed values of $\mathbf{Q}$ at the interface.

The reconstruction of the characteristic variables using the CRWENO scheme requires the coupled solution of all three components. At interface $x_{i+1/2}$, the eigenvalues ($\lambda^k_{i+1/2}$), left eigenvectors ($\mathbf{l}^k_{i+1/2}$) and right eigenvectors ($\mathbf{r}^k_{i+1/2}$) are computed from the Roe-averaged state, where k is the index denoting each characteristic field. The k-th characteristic flux at the j-th cell is expressed as

$$\alpha^k_j = \mathbf{l}^k_{i+1/2} \cdot \mathbf{F}(x_j) \tag{22}$$

The CRWENO5 scheme, given by Eq. 20, is applied to the characteristic fluxes to yield a block tridiagonal system of equations, expressed as

$$
\begin{aligned}
& a(l_{k1}\hat{F}^L_{1,j-1/2} + l_{k2}\hat{F}^L_{2,j-1/2} + l_{k3}\hat{F}^L_{3,j-1/2}) \\
+ \quad & b(l_{k1}\hat{F}^L_{1,j+1/2} + l_{k2}\hat{F}^L_{2,j+1/2} + l_{k3}\hat{F}^L_{3,j+1/2}) \quad = \hat{a}\alpha^k_{j-1} + \hat{b}\alpha^k_j + \hat{c}\alpha^k_{j+1} \\
+ \quad & c(l_{k1}\hat{F}^L_{1,j+3/2} + l_{k2}\hat{F}^L_{2,j+3/2} + l_{k3}\hat{F}^L_{3,j+3/2})
\end{aligned}
\tag{23}
$$

where l_{k1}, l_{k2}, l_{k3} are the components of the left eigenvector $\mathbf{l}^k_{j+1/2}$ and $\hat{F}^L_{1,j+1/2}, \hat{F}^L_{2,j+1/2}, \hat{F}^L_{3,j+1/2}$ are the components of the flux vector $\hat{\mathbf{F}}^L_{j+1/2}$. The right-biased characteristic flux, $\hat{\alpha}^{R,k}$, can be similarly computed and the Roe-Fixed (RF) formulation[5,8] is used to compute the upwind characteristic flux from the left and right biased approximations,

$$
\hat{\alpha}^k_{j+1/2} =
\begin{array}{l}
\hat{\alpha}^{L,k}_{j+1/2} \text{ if } \lambda_{j,j+1/2,j+1} > 0 \\
\hat{\alpha}^{R,k}_{j+1/2} \text{ if } \lambda_{j,j+1/2,j+1} < 0 \\
\frac{1}{2}[\hat{\alpha}^{L,k}_{j+1/2} + \hat{\alpha}^{R,k}_{j+1/2} + \lambda_{max}(\hat{v}^{L,k}_{j+1/2} - \hat{v}^{R,k}_{j+1/2})] \text{ else}
\end{array}
\tag{24}
$$

American Institute of Aeronautics and Astronautics

where $\lambda_{max} = \max(\lambda_{j,j+1/2,j+1})$ and $v_j^k = \mathbf{l}_{i+1/2}^k \cdot \mathbf{Q}(x_j)$ is the characteristic state vector.

The computational expense for the CRWENO scheme has been discussed[18] and they have been demonstrated to be more efficient than WENO schemes for scalar reconstruction. Although the computational expense is higher for a given grid resolution, the CRWENO scheme achieves the same accuracy and resolution on coarser meshes. The characteristic-based reconstruction is significantly more expensive due to a block tridiagonal inversion and the size of the block increases with the number of dimensions. Numerical solutions of inviscid flows with strong shocks require the characteristic-based reconstruction for robust, non-oscillatory solutions. However, it is observed in this study that the reconstruction of conserved and primitive variables yields non-oscillatory solutions for viscous flows. Thus, the CRWENO reconstruction of conserved/primitive variables results in an algorithm with improved spectral resolution and lower numerical cost (for the same accuracy).

V.   Results and Validation

V.A.   Inviscid Euler Equations

The order of convergence and the accuracy of the CRWENO5 scheme, compared to those of the WENO5 scheme, is demonstrated by considering a smooth, linear problem. The advection of a density wave is considered. The solution at any time is given by

$$
\begin{aligned}
\rho(x,t) &= \rho_\infty + A\sin[\pi(x - u_\infty t)] \\
u(x,t) &= u_\infty \\
p(x,t) &= p_\infty
\end{aligned}
\tag{25}
$$

The freestream conditions are taken as $\rho_\infty = u_\infty = p_\infty = 1$ and the amplitude of the density wave is taken as $A = 0.1$. The domain is $[0,2]$ and discretized with a uniform grid. Periodic boundary conditions are enforced at both boundaries. The solution is obtained after one cycle at $t = 2$ and the errors calculated.

Table 1. L_2 Convergence Rates for Entropy Wave Advection

N	WENO5 Error	r_c	CRWENO5 Error	r_c
15	1.028E-04	-	1.900E-05	-
30	2.988E-06	5.10	3.946E-07	5.59
60	9.325E-08	5.00	1.084E-08	5.19
120	2.917E-09	5.00	3.172E-10	5.10
240	9.098E-11	5.00	9.599E-12	5.05

The problem is solved using the WENO5 and CRWENO5 schemes with TVD-RK3 time-stepping. An initial grid of 15 points is refined successively. The initial CFL (for the grid of 15 points) is 0.1 and is reduced by a factor of $2/(2^{5/3})$ at each refinement (since the spatial interpolation is fifth order and time marching is third order, this ensures that time discretization errors converge at the same rate as the space discretization ones). Table 1 shows the errors and orders of convergence for the two schemes with conserved variable based reconstruction. The errors for the CRWENO5 scheme are an order of magnitude lower than the WENO5 scheme, for the same order of convergence.

The initial conditions of the Lax shock tube[27] are given by

$$
\begin{aligned}
\rho_L, u_L, p_L &= 0.445, 0.698, 3.528 \\
\rho_R, u_R, p_R &= 0.5, 0, 0.571
\end{aligned}
\tag{26}
$$

The domain is taken as $[0,2]$ and the initial discontinuity is located at $x = 1$. The solution is evolved in time using the TVD-RK3 time-stepping till $t = 0.2$ at a CFL of 0.5. Zero-gradient boundary conditions are applied at both boundaries. Figure 2(a) shows the solutions obtained by the WENO5 and CRWENO5 schemes on a grid with 80 points. Mapping of the WENO weights is used to improve the resolution of the discontinuities. The exact solutions are obtained by a Riemann solver.[2] The compact schemes are seen to be

American Institute of Aeronautics and Astronautics

non-oscillatory, thus showing that the smoothness indicators of the WENO5 scheme work well with compact stencils. It can be observed that the shock and the contact discontinuity are significantly less smeared for the CRWENO5 scheme compared to the WENO5 scheme. This is expected since the compact schemes have lower dissipation error and better spectral properties than explicit interpolation.
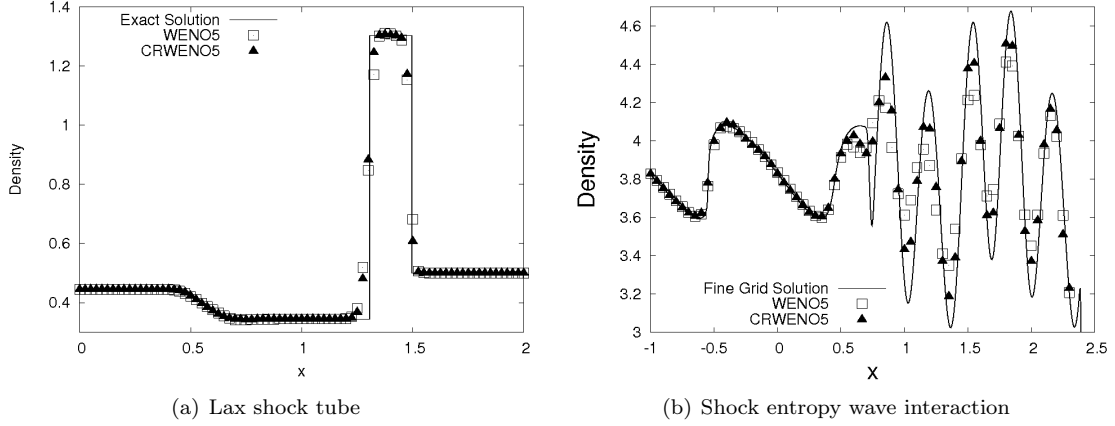

(a) Lax shock tube   (b) Shock entropy wave interaction

Figure 2. One-dimensional inviscid flow problems

The interaction of a shock wave with a density wave[5] is simulated. The initial conditions consist of a shock wave, which interacts with a density wave to generate a solution consisting of high-frequency smooth structures as well as discontinuities. The density fluctuations are amplified as they pass through the shock. Thus, the problem is a good test to assess the non-oscillatory behavior of the scheme while resolving high-frequency smooth waves. In the present study, the initial conditions consist of a Mach 3 shock and a density wave[9] and are given by

$$
\begin{aligned}
(\rho, u, p) &= (\frac{27}{7}, \frac{4\sqrt{35}}{9}, \frac{31}{3}) \text{ if } x < -4 \\
&= (1 + \frac{1}{5}\sin 5x, 0, 1) \text{ if } x \geq -4
\end{aligned}
\tag{27}
$$

The domain is taken as $[-5, 5]$ and zero-gradient boundaries are applied at both boundaries. The solution is obtained at $t = 1.8$ at a CFL of 0.1. The TVD-RK3 time-stepping is used. Figure 2(b) shows the density on a grid with 200 points for the WENO5 and CRWENO5 schemes using a characteristic-based reconstruction, magnified around the post-shock high-frequency waves. Mapping of the WENO weights is used for both the WENO5 and CRWENO5 schemes to improve the resolution of the solution. The "Fine Grid Solution" refers to the solution obtained by the WENO5 scheme on a grid with 2000 points and is used as the reference solution in absence of an exact one. The CRWENO5 scheme yields solutions with sharper resolution of the high-frequency waves and non-oscillatory behavior across discontinuities. This demonstrates the ability of the compact schemes to non-oscillatory solutions with higher resolution and lower dissipation, compared to the traditional WENO schemes.

V.B.   Isentropic Vortex Convection

The long-term, inviscid convection of an isentropic vortex[28] is solved and the CRWENO5 scheme is compared with the WENO5 scheme. The domain is $[0, 10] \times [0, 10]$ and the freestream flow is $\rho_\infty = 1, u_\infty = 0.5, v_\infty = 0, p_\infty = 1$. The vortex, initially centered at $(x_c, y_c) = (5, 5)$, is specified as,

$$
\begin{aligned}
\rho &= \left[1 - \frac{(\gamma - 1)b^2}{8\gamma\pi^2}e^{1-r^2}\right]^{\frac{1}{\gamma-1}} \; ; \; p = \rho^\gamma \\
\delta u &= -\frac{b}{2\pi}e^{\frac{1-r^2}{2}}(y - y_c) \\
\delta v &= \frac{b}{2\pi}e^{\frac{1-r^2}{2}}(x - y_c)
\end{aligned}
\tag{28}
$$

where $r = ((x - x_c)^2 + (y - y_c)^2)^{1/2}$ is the distance from the vortex center and $b = 0.5$ is the vortex strength. All boundaries are periodic and the time period is $T_p = 20$.
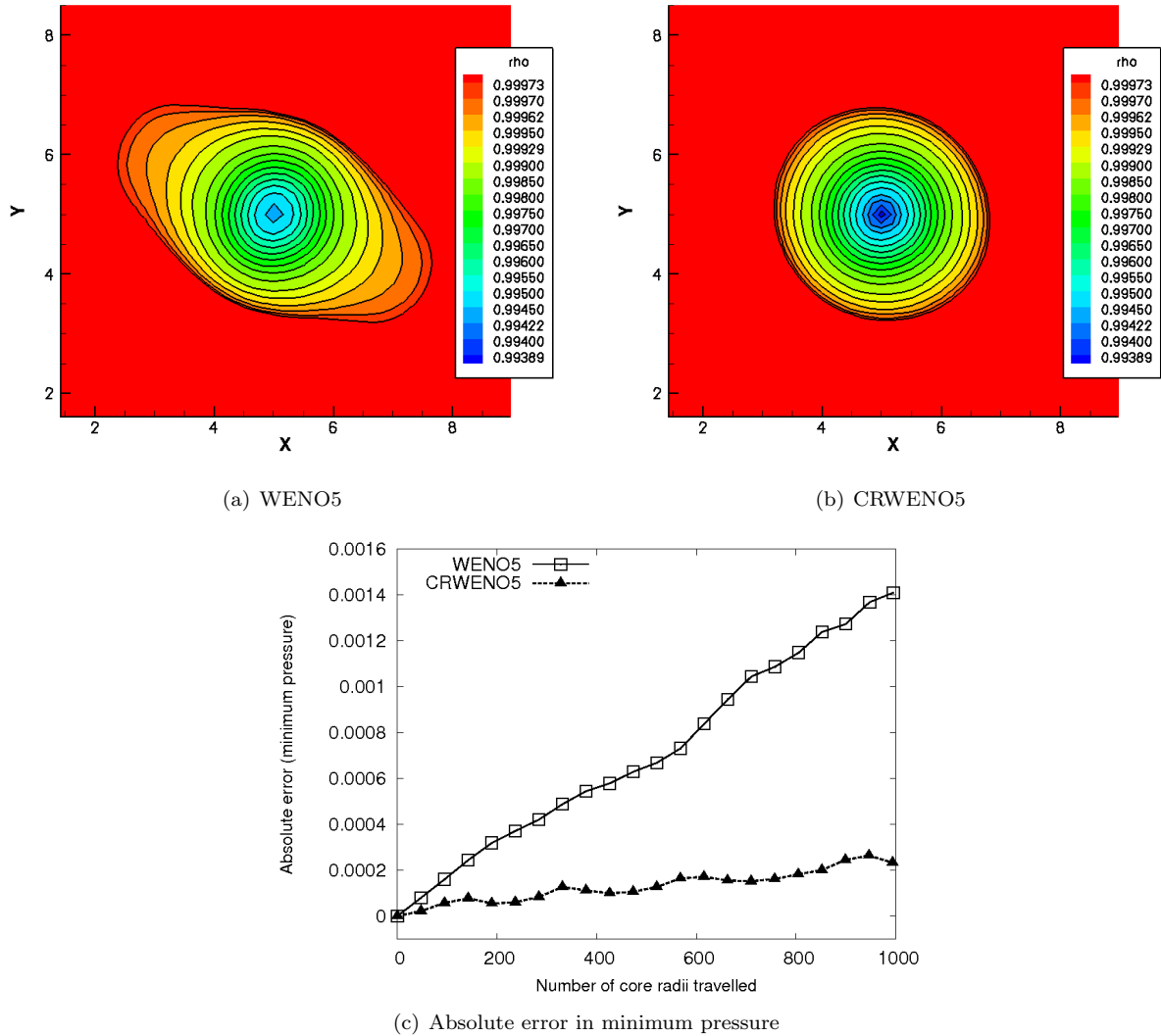

(a) WENO5

(b) CRWENO5

(c) Absolute error in minimum pressure

Figure 3. Density contours and vortex core pressure error for convection over 1000 core radii

Figures 3(a) and 3(b) show the density contours for the solutions on a 60×60 grid and CFL number of 0.5. The solutions are obtained using the WENO5 and CRWENO5 schemes with TVD-RK3 time-stepping. A significant improvement is observed with the CRWENO5 scheme in preserving the vortex shape and strength for long-term convection. The absolute error (non-dimensionalized) in minimum pressure at the vortex core is shown in figure 3(c) and the CRWENO5 yields a solution with lower error than the WENO5 scheme.

V.C. Sound Generation from Shock Vortex Interaction

The sound generation from the interaction of a planar shock wave with a vortex is simulated to verify the ability of the algorithm to accurately capture acoustic signals. The nature of the interaction and the resulting acoustics depend on the strengths of the shock wave as well as the vortex. The "strong" interaction is characterized by a multi-stage process, where the primary collision of the vortex with the shock wave is sufficiently strong to produce secondary shock structures that subsequently interact with the vortex. In this study, a strong interaction is simulated which results in the generation of three sounds.

A large domain ($[-70, 10] \times [-40, 40]$) is taken such that the sound waves do not reach the boundaries within the duration of interest. The initial conditions consist of a stationary Mach 1.2 shock at $x = 0$
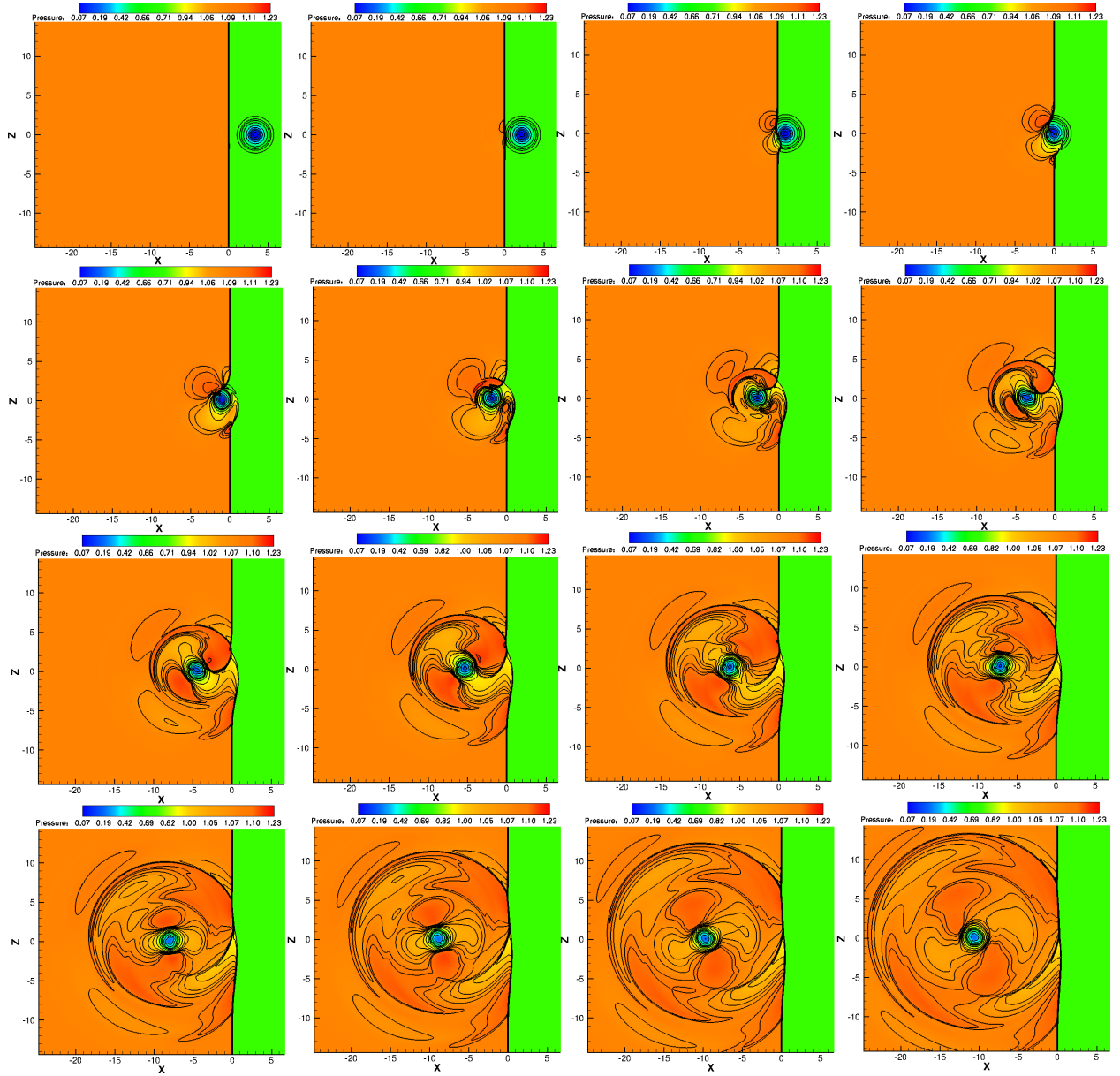
Figure 4. Pressure contours for the interaction of a stationary shock with a vortex

with the flow going from right to left. The right $(x = 10)$ boundary is supersonic inflow while post-shock flow conditions are maintained at the left $(x = -70)$ boundary. The top $(y = 40)$ and bottom $(y = -40)$ boundaries are periodic. An isentropic vortex is initialized at $(x_c = 4, \; y_c = 0)$ for which the density and velocity is given by

$$
\begin{aligned}
\rho &= \left(1 - \frac{1}{2}(\gamma - 1)M_v^2 e^{1-r^2}\right)^{\frac{1}{\gamma-1}} \\
\delta u &= -M_v e^{\frac{1}{2}(1-r^2)}(y - y_c) \\
\delta v &= M_v e^{\frac{1}{2}(1-r^2)}(x - x_c)
\end{aligned}
\tag{29}
$$

The vortex strength M_v is taken as 1.0. The simulation time is non-dimensionalized by the vortex core radius and the speed of sound upstream of the shock and the simulation is run till a non-dimensional time of 16. The Reynolds number is taken as 800.

Figure 4 shows the pressure contours for this flow. The solution is obtained on a 640×640 uniform

American Institute of Aeronautics and Astronautics

(a) Azimuthal - Precursor ($r/R = 16.0$), 2nd Sound ($r/R = 12.0$), 3rd Sound ($r/R = 6.7$)
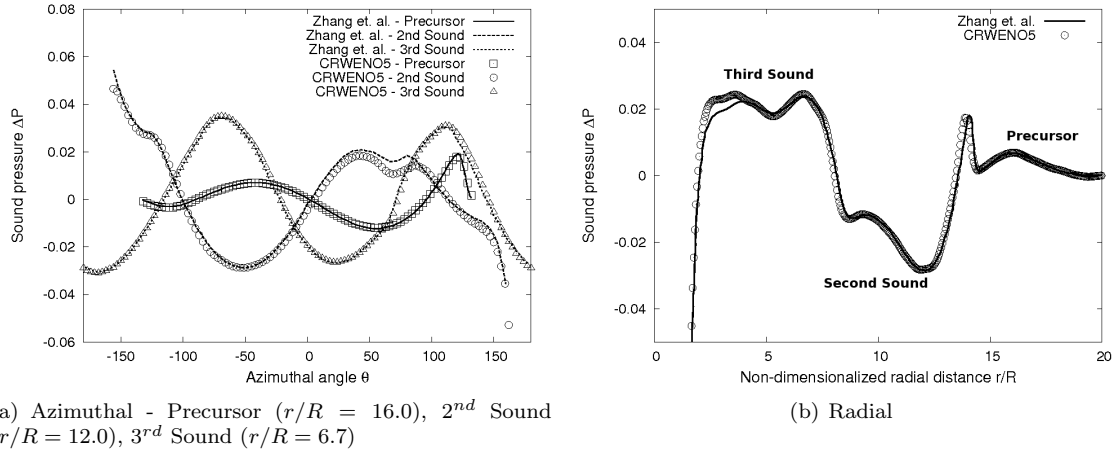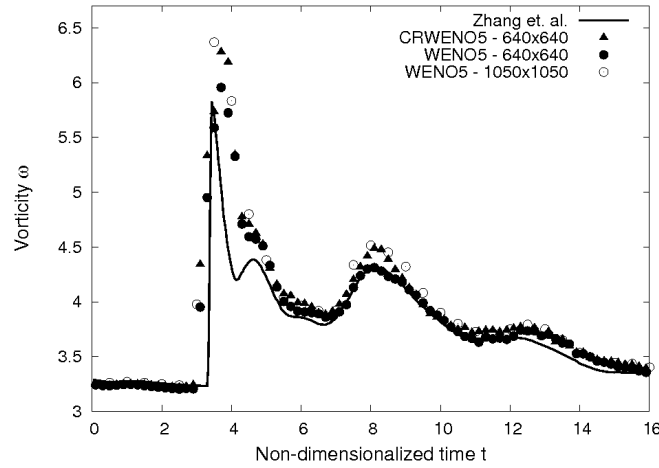
(b) Radial

Figure 5. Sound pressure at $t = 16$

Figure 6. Vorticity at vortex core vs. time

grid with CRWENO5 scheme and TVD-RK3 time-stepping. The time step size dt is taken as 0.005. The initial impact of the vortex with the shock results in shock deformation and regions of compression and rarefaction are formed, as seen in the third figure. As the vortex passes through the shock, the compression and rarefaction regions grow and two more such regions are formed (as seen in the fifth and sixth figures) to form an alternating compression-rarefaction flow pattern. Thus, the primary interaction of the vortex with the shock wave results in the emission of a quadrupolar sound wave, referred to as the precursor. The shock deformation caused by the vortex causes the creation of curved shock stems above the vortex that are visible in the subsequent figures. The interaction of the vortex with these secondary shock structures causes the emission of two more sound waves, each of which are quadrupolar in nature and out of phase with each other.

Figure 5 shows the radial and azimuthal sound pressure (ΔP) around the vortex at $t = 16$. The sound pressure is defined as the difference between the actual pressure and the post-shock pressure, normalized by the post-shock pressure. The radial sound pressure variation is shown for a line extending from the center of the vortex at an angle of 45° (clockwise) from the negative x-axis. Our results are verified with previous computational studies[29] which were obtained using the fifth order WENO scheme and a good agreement is observed. Figure 5(b) shows the three sounds that are generated - precursor, second and third sounds. The pressure peak observed between the precursor and the second sound is the secondary shock stem.

The evolution of the vorticity magnitude at the vortex core is shown in figure 6. Our results with the CRWENO5 scheme on a 640×640 grid are compared with those obtained by Zhang, et. al.[29] on a clustered grid with a comparable resolution. In addition, results obtained using the fifth order WENO

scheme (WENO5) is shown for two grid resolutions - 640×640 and 1050×1050. The first peak, at $t = 3.5$, is due to interaction of the vortex with the primary shock wave, while a subsequent increase in vorticity is seen around $t = 8$ due to the interaction with the secondary shock stems. While a good agreement is seen between the different results, the CRWENO5 scheme shows a significant improvement in capturing the primary and secondary interactions of the vortex with the shocks, compared to the WENO5 scheme at the same grid resolution. The results obtained by the CRWENO5 scheme on the 640×640 grid compare well with those obtained by the WENO5 scheme on the 1050×1050 grid.

V.D.   Steady Flow around RAE2822 Airfoil

The algorithm is validated for flows involving curvilinear meshes by solving the steady, turbulent flow around the RAE2822 airfoil. The computational results are validated with experimental data available in the literature.[30] The domain is discretized by a body-fitted 521×171 C-type mesh with the outer boundary 50 chord-lengths away. Experimental data is available for a Reynolds number of 6.5 million with the airfoil at $2.92°$ angle of attack and the freestream Mach number as 0.725.[30] The experiment was carried out inside a wind tunnel and the flow conditions for the two-dimensional computational study are corrected to an angle of attack of $2.51°$ and a freestream Mach number of 0.731.[31]
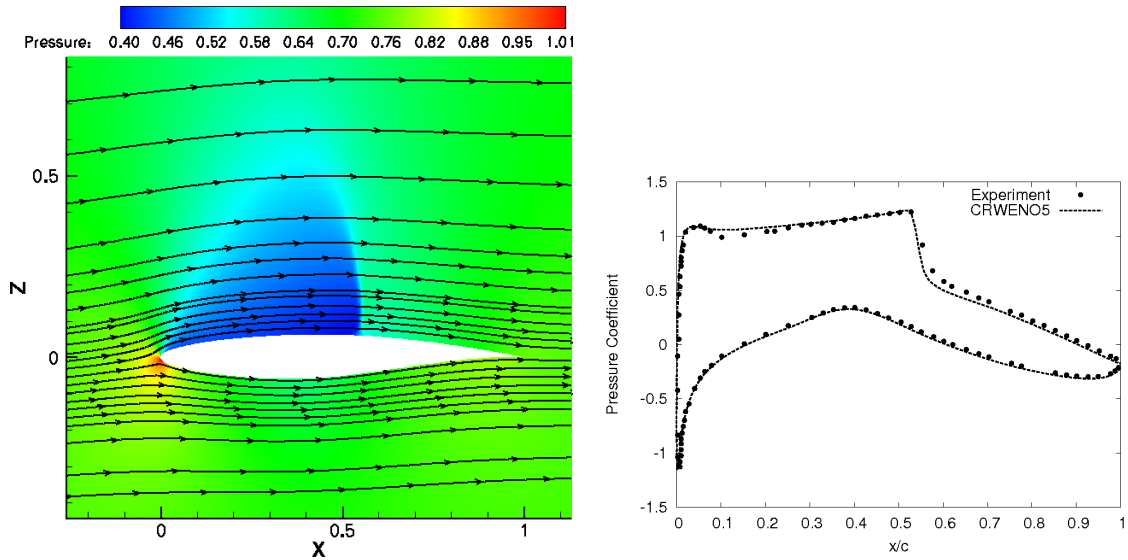

Figure 7.   Flowfield and pressure distribution around the RAE2822 airfoil
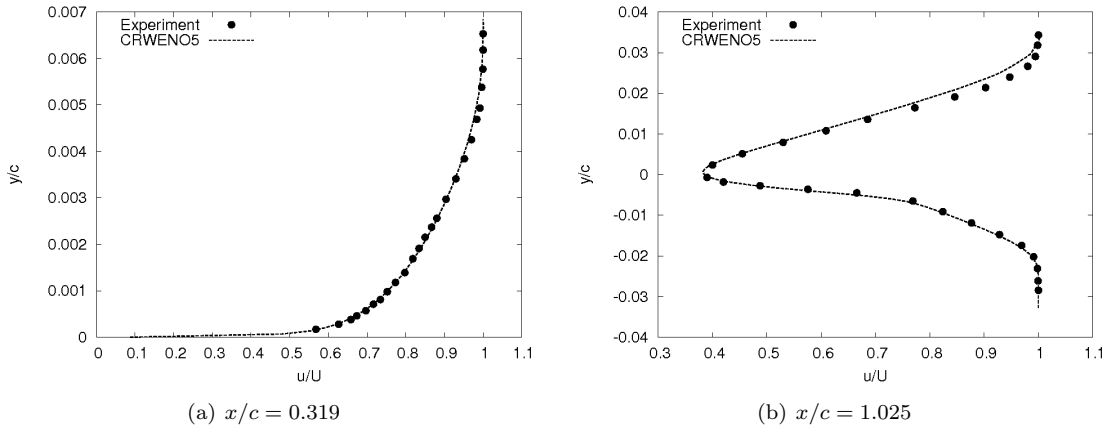

(a) $x/c = 0.319$

(b) $x/c = 1.025$

Figure 8.   Velocity profiles in boundary layer and wake for the RAE2822 airfoil

The solution is obtained using the CRWENO5 scheme and BDF2 time-stepping. Figure 7(a) shows the pressure distribution and the streamlines for the flow. The surface pressure coefficient distribution is
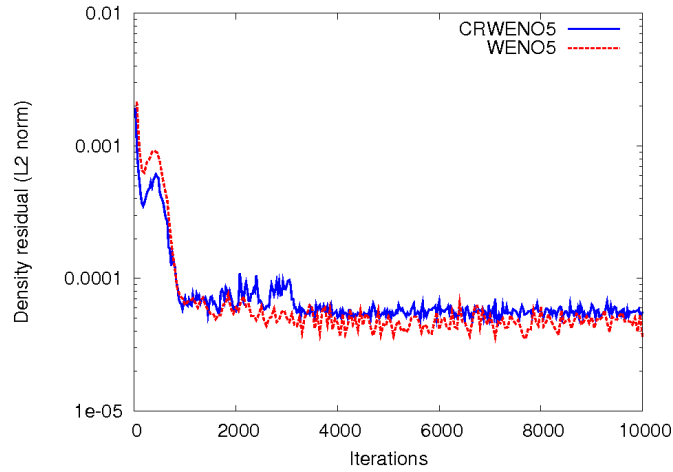
American Institute of Aeronautics and Astronautics

Figure 9. Convergence history for the CRWENO5 and WENO5 schemes

shown in figure 7(b) and validated with experimental data.[30] The velocity profiles in the boundary layer and the wake are shown in figure 8 at chord-wise stations $0.319c$ and $1.025c$ respectively. A good agreement is observed with the experimental data for the surface pressure and the velocity profiles. The convergence histories of the CRWENO5 and WENO5 schemes are shown in figure 9 and both these schemes show a residual drop of only one-and-a-half orders of magnitude. A component-wise reconstruction is used in the present study, along with the WENO weights as formulated by Jiang and Shu. The convergence of the WENO schemes for airfoil problems has been studied[32] and non-characteristic formulations were observed to show poor convergence. Although the current results agree well with experimental data, the authors are currently investigating the improvement of convergence behavior for the CRWENO5 scheme.
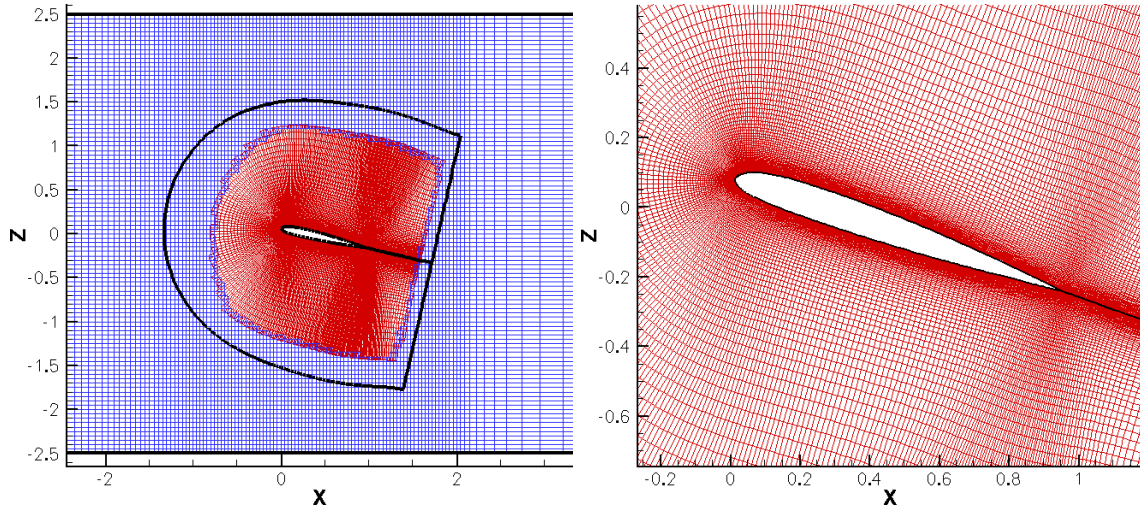

Figure 10. Overset airfoil and wind tunnel meshes for SC1095 dynamic stall case

V.E. Dynamic Stall of SC1095 Airfoil

The numerical solution of flows on a domain with overset meshes requires the determination of regions of overlap, where the solution is transferred between the meshes, along with blanked out regions inside of physical bodies as well as to minimize the region of overlap. The solution update procedure is such that at a given instant in time, the solution update at a blanked out point is zero. This may create a locally unphysical solution; but as it does not influence interior field points (since it is separated by points that use interpolated data) it does not contaminate the solution field. In addition, if a blanked point becomes a field point at a future point in time, there will always be a transition period where the data will be updated
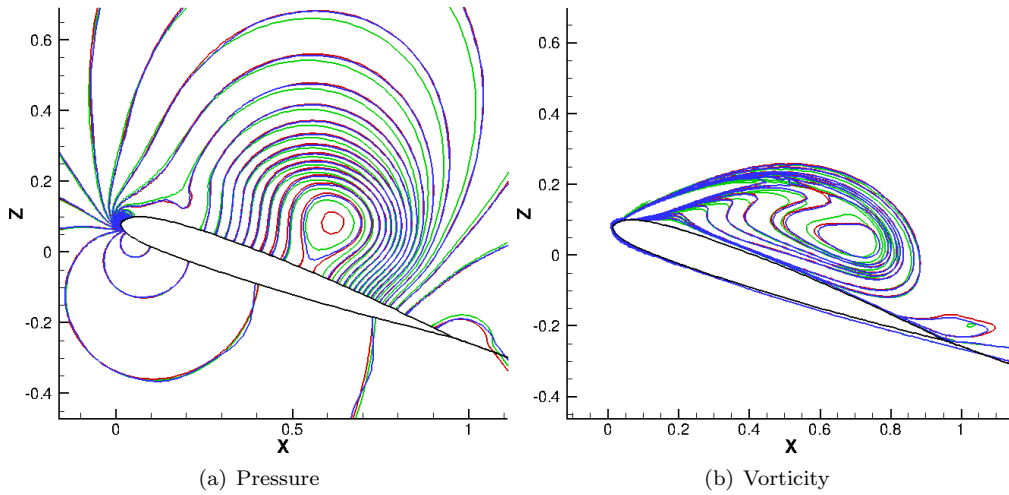
American Institute of Aeronautics and Astronautics

(a) Pressure

(b) Vorticity

Figure 11. Comparison of pressure and vorticity contours for different schemes - MUSCL3 (green), WENO5 (red) and CRWENO5 (blue)
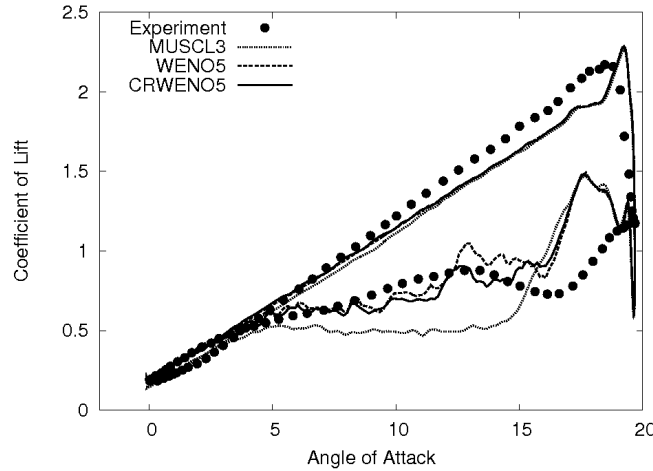

Figure 12. Lift coefficient vs. angle of attack – Validation with experimental results

using interpolated data from another mesh. A compact scheme results in a coupling of the interpolated interface fluxes with neighboring fluxes and therefore, the treatment of the fluxes in the blanked out region is important. For the current WENO-based compact scheme, it is expected that the non-smooth solution across the blanked out region will result in the adaptive stenciling of the CRWENO scheme biasing away from the blanked out region (since it is similar to a discontinuity) and result in a decoupling of the blanked out region from the field and interpolated points. Thus, the CRWENO scheme should produce smooth solutions across the overlap region, similar to non-compact schemes.

The dynamic stall of a SC1095 airfoil in a wind tunnel is simulated using the CRWENO5 scheme and the results are verified with those obtained using non-compact schemes like the third order MUSCL scheme (MUSCL3) and the fifth order WENO scheme (WENO5). The second order Backward Differencing (BDF2) is used to march the solution in time with 15 Newton sub-iterations for time accuracy. The wind tunnel height is taken as $5c$ where c is the airfoil chord. A 365×138 C-mesh is used for the airfoil while a 151×101 Cartesian mesh, that is clustered near the airfoil, is used for the wind tunnel. Figure 10 shows the overset domain and the mesh around the airfoil.

The simulation is run at a Reynolds number of 3.92 million and a freestream Mach number of 0.302. The mean angle of attack is 9.78º and the pitching amplitude is 9.9º with a reduced frequency of 0.099. A time step of $dt = 0.01$ is taken which results in 10500 iterations per cycle. The simulation is run for four complete cycles and the solutions from the last cycle are compared. Figure 11 compares the pressure and vorticity
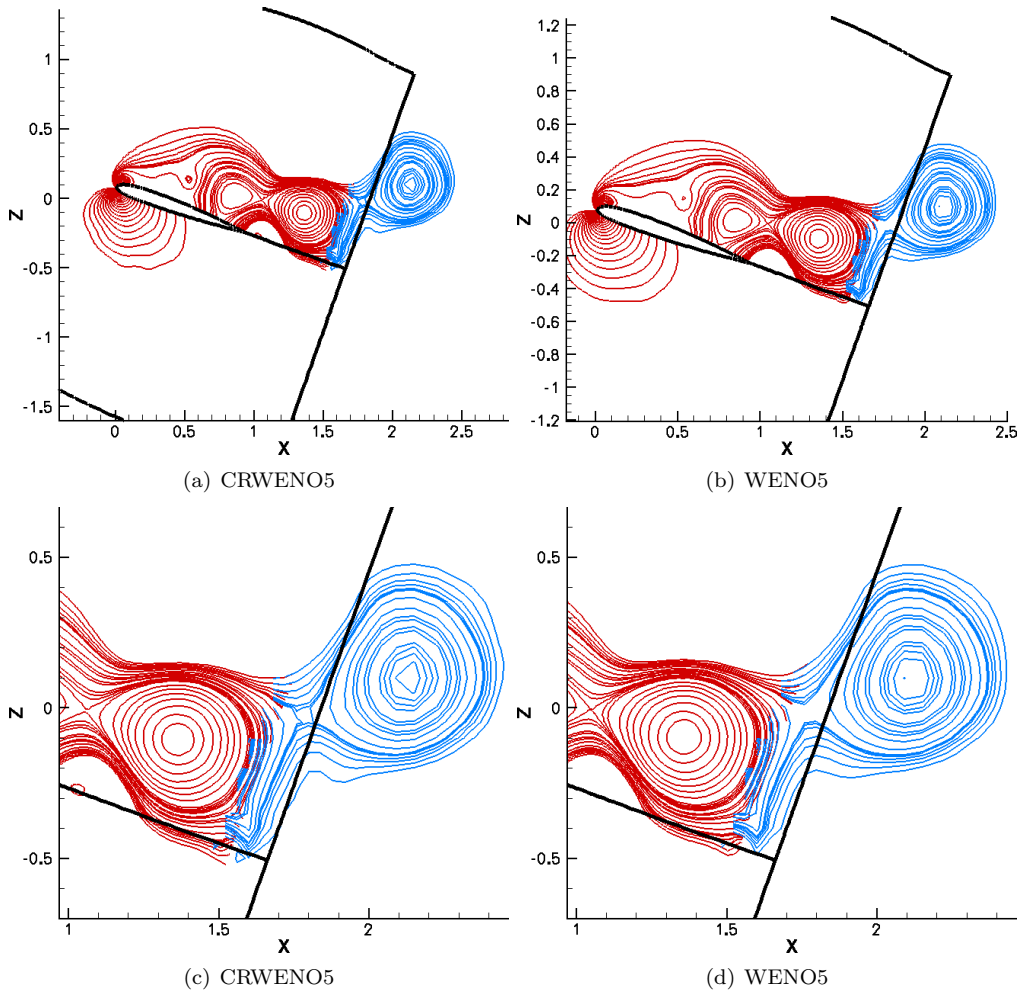
American Institute of Aeronautics and Astronautics

Figure 13. Comparison of pressure contours at 18.83° angle of attack for the overlap region - airfoil mesh (red) and wind tunnel mesh (blue)

contours for the MUSCL3, WENO5 and CRWENO5 schemes. The solutions are obtained at 18.94º angle of attack (upstroke). The figure shows the leading edge vortex after it has detached from the leading edge and has started convecting downstream. The solution obtained using the CRWENO5 scheme agrees with those obtained using the non-compact schemes. The coefficient of lift as a function of the angle of attack is shown for one complete cycle in figure 12. The numerical results are compared with experimental data[33] and a good agreement is seen. Figures 13(a) and 13(b) show the pressure contours for the flow when the airfoil is at 18.83º angle of attack (upstroke). The solutions for the compact scheme and non-compact WENO5 scheme are shown. The vortices shed from the upper surface are transferred from the airfoil mesh to the wind tunnel mesh as they convect downstream. A magnified view of the overlap region between the two meshes for the two schemes is shown in figures 13(c) and 13(d). The contours on the airfoil and wind tunnel meshes agree with each other in the overlap region and are continuous across the mesh boundary. Thus, the applicability of the compact scheme is verified for overset meshes requiring transfer of flow data between domains.

V.F. Flow around Pitching-Plunging NACA0005 Airfoil

Flow around a pitching-plunging airfoil at low Reynolds number is representative of the flowfield around a flapping-wing-based micro-air vehicle and has been previously studied using experimental and numerical techniques.[34] The combined pitching and plunging motion results in positive thrust (negative drag) when averaged over one cycle. Previous computational studies used Reynolds-Averaged Navier-Stokes (RANS) based algorithms with second order spatial accuracies. In the present study, an attempt is made to capture the finer details of the flowfield near the airfoil surface. The one-equation Spalart-Allmaras turbulence model[25]
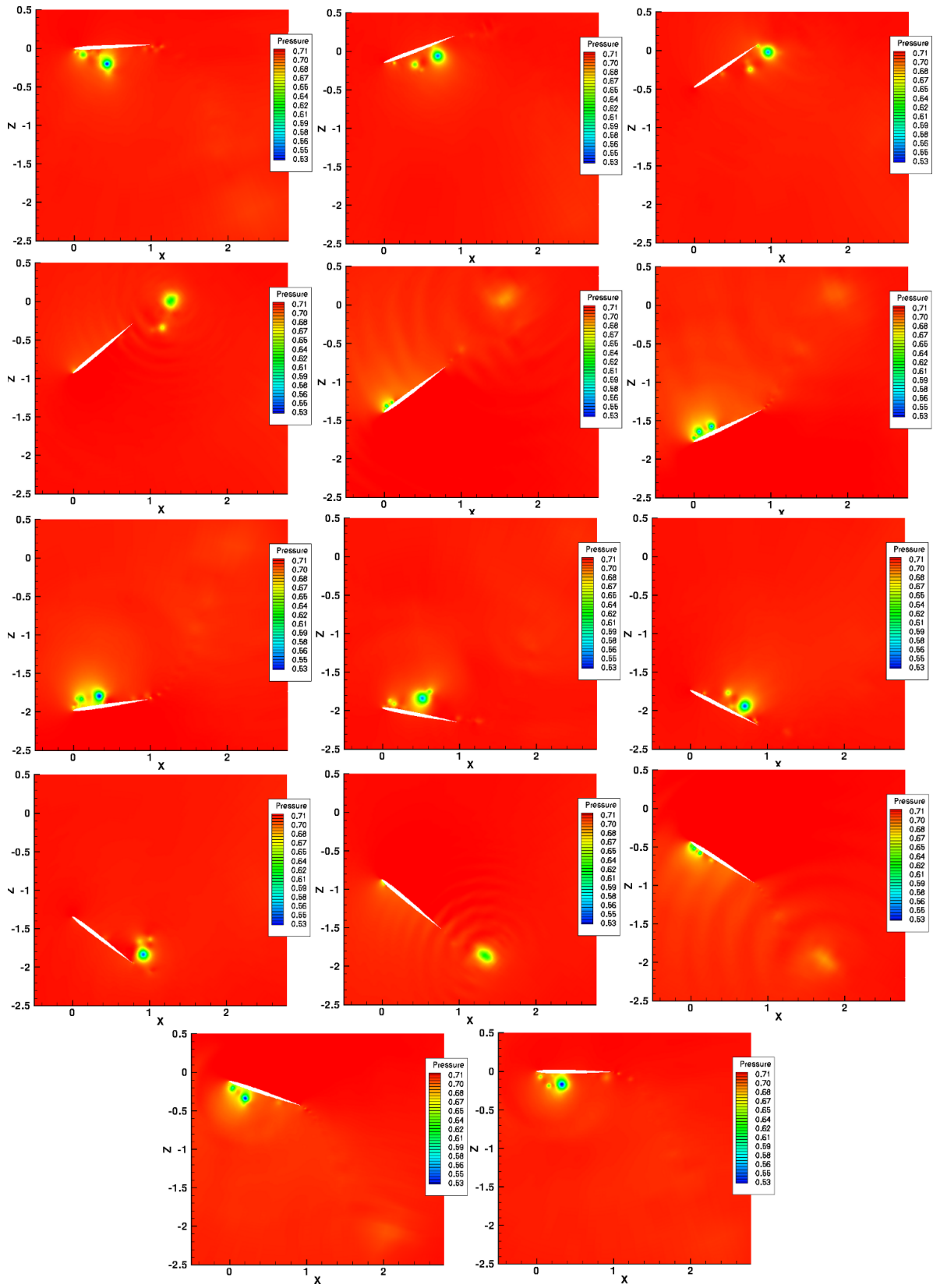
American Institute of Aeronautics and Astronautics

Figure 14. Pressure distribution over one time period

American Institute of Aeronautics and Astronautics

(a) Lift   (b) Drag
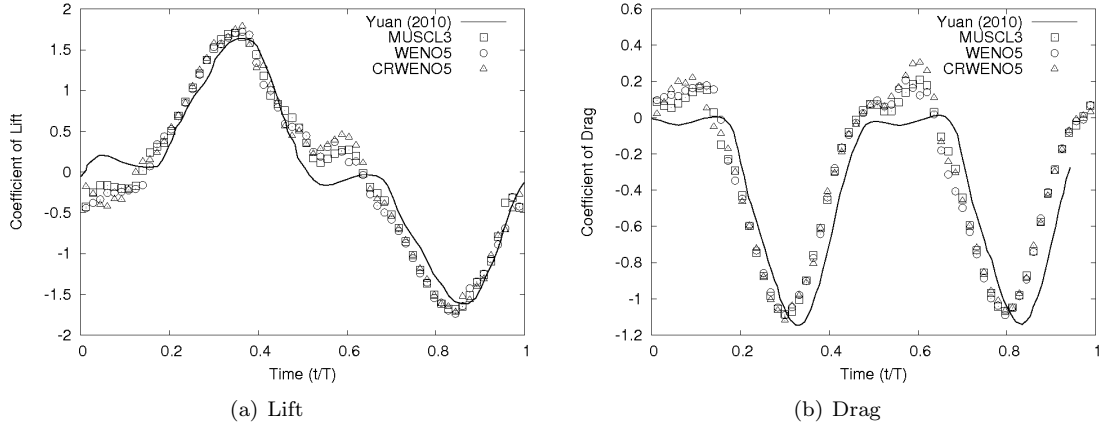
Figure 15. Integrated forces over one time period

(a) MUSCL3   (b) WENO5   (c) CRWENO5
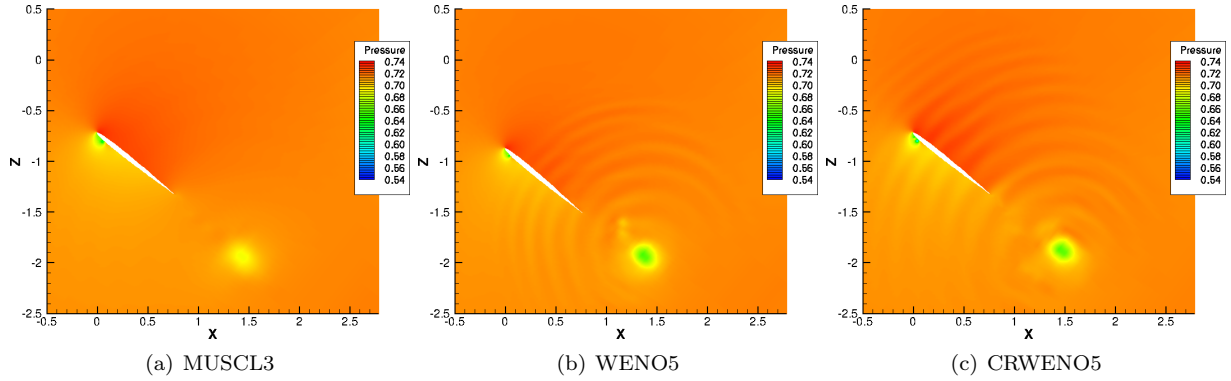
Figure 16. Pressure distribution for different schemes at $t/T = 0.75$ (Upstroke)

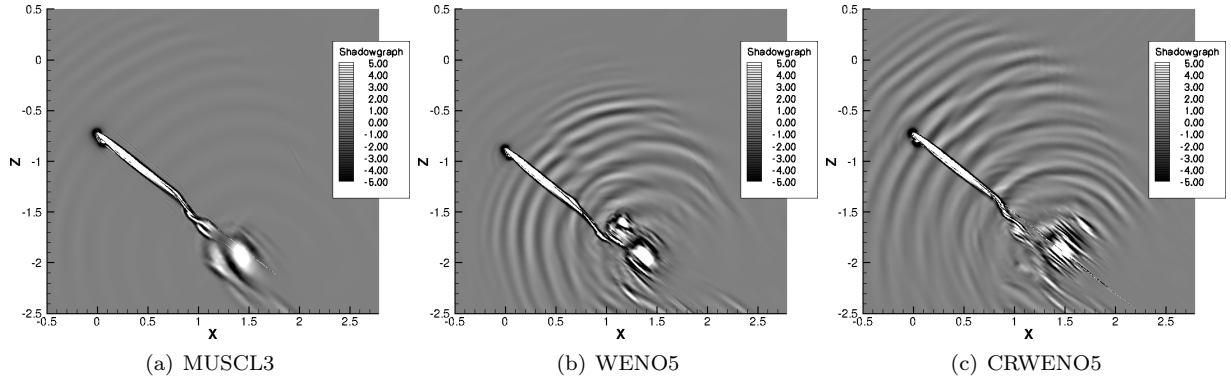(a) MUSCL3   (b) WENO5   (c) CRWENO5

Figure 17. Numerical shadowgraph for different schemes at $t/T = 0.75$ (Upstroke)

is used with the Delayed-Detached Eddy Simulation (DDES) modification in its two-dimensional form to resolve coherent vortical structures. The fifth order CRWENO scheme is used for spatial reconstruction, along with the third order MUSCL and fifth order WENO schemes.

The domain is discretized using a 391×161 C-type mesh. A freestream Mach number of 0.1 is specified and the Reynolds number is 15000. The pitching motion is specified by a pitch amplitude of 40° around a zero mean angle of attack and a reduced frequency of 0.795. The plunging motion has an amplitude of 1.0 and the same reduced frequency. The plunging motion is $\pi/2$ behind in phase than the pitching motion and the airfoil pitches around the leading edge. The simulation is run over four cycles and the results from the final cycle are presented. Figure 14 shows the pressure distribution around the airfoil over one complete cycle. The solutions are obtained using the CRWENO5 scheme. As the airfoil plunges downwards, leading
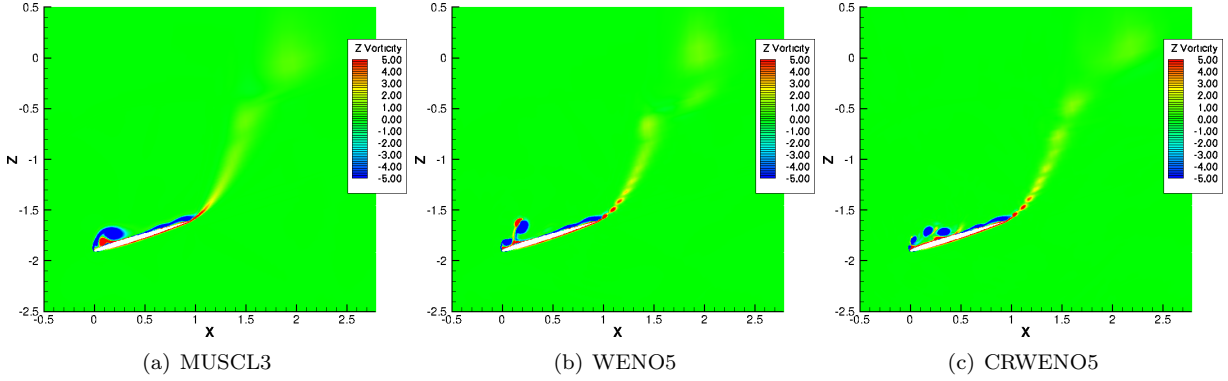
American Institute of Aeronautics and Astronautics

Figure 18. Vorticity distribution for different schemes at $t/T = 0.40$ **(Downstroke)**

edge vortices are formed on the upper surface that grow in size and then detach from the surface. This results in a positive lift during the downstroke. Similarly, vortices form and shed from the lower surface during the upstroke resulting in negative lift. Both strokes result in negative drag and the flapping motion causes the generation of positive thrust. The lift and drag variation over one cycle is shown in figure 15. Results from the CRWENO5, WENO5 and the MUSCL3 schemes are verified with the previous computational results[34] where the flow was solved using an incompressible, RANS-based algorithm with second order accuracy in time and space. The integrated forces agree well with the previous results.

The pressure and the numerical shadowgraph ($\nabla^2 \rho$) for the solution at $t/T = 0.75$ are shown in figures 16 and 17. Acoustic waves are observed that result from the interaction of the shed vortices with the airfoil. The CRWENO5 scheme is compared with the MUSCL3 and WENO5 schemes and all three solutions use the two-dimensional DDES turbulence model. The CRWENO5 scheme shows a significant improvement in the resolution of the acoustic waves, compared to the WENO scheme of the same order of accuracy. Although the vortex is accurately captured by the WENO5 and CRWENO, as seen by the pressure (or density, which is not shown here), oscillations are seen in the second derivative of the density (as seen by the shadowgraph). This is due to the choice of the weights for the non-linear limiting of the WENO algorithm and the improvement of this behavior is a subject of current research.

Figure 18 shows out-of-plane vorticity at $t/T = 0.4$ for the three schemes. It is observed that the CRWENO5 scheme is able to resolve the different vortices that form and detach from the airfoil surface. A comparison of the three schemes show that while a second or third order scheme is sufficient to predict the integrated forces like the lift and drag, a higher order scheme is necessary to capture the flow features near the airfoil surface as well as acoustic waves generated from the pitching-plunging motion. Although the CRWENO5 and WENO5 schemes are both fifth order accurate, the increased spectral resolution capabilities of the compact scheme yields a solution with higher resolution of the flow features than the non-compact scheme.

VI.   Conclusions

A new class of high order accurate non-oscillatory schemes with high spectral resolution has been previously introduced by the authors. The CRWENO scheme is based on applying the WENO algorithm of solution-dependent adaptive stenciling to compact interpolation schemes. At each interface, lower-order compact interpolation stencils are identified and combined using WENO weights. The weighted combination results in a higher-order compact scheme at smooth regions of the solution and a non-oscillatory biased compact scheme across discontinuities. The performance of the new scheme, in terms of accuracy, convergence and resolution, has been analyzed for the scalar conservation law and the inviscid Euler equations, and compared to that of the WENO schemes of Jiang and Shu. The CRWENO scheme yielded solutions with lower absolute errors for smooth problems, when compared with the WENO scheme of the same order of convergence, thus being computationally more efficient. The higher resolution and lower dissipation of the CRWENO scheme also resulted in reduced smearing of discontinuities and improved preservation of waveforms for long-term convection.

The present paper demonstrates the application of the CRWENO scheme to the Navier-Stokes equations

to simulate viscous, turbulent flows representative of practical problems. The order of convergence and the accuracy of the new scheme is demonstrated by solving the linear advection of a density wave. Two canonical test cases, the Lax shock tube and the Shu-Osher test case, are presented to demonstrate the improved spectral resolution and reduced dissipation of the CRWENO scheme, for problems containing discontinuities as well as high-frequency waves. The inviscid convection of an isentropic vortex is solved and the CRWENO scheme shows a significant improvement in preserving the vortex strength and shape over large convection times. The sound generation from the interaction of a shock wave with a vortex is simulated and the results obtained are verified with previous computational studies. An improvement is seen in the capturing of the shock-vortex interaction using the CRWENO scheme, which yielded solutions comparable to the WENO scheme on a finer mesh. The algorithm is validated for the steady flow around the RAE2822 airfoil where the domain is discretized by a curvilinear C-type mesh. The surface pressure coefficient and the boundary layer and wake velocity profiles are compared with experimental data and a good agreement is observed. The dynamic stall of the SC1095 airfoil is simulated to verify the algorithm for a domain composed of an overset mesh system with relative grid motion. Results from the compact scheme are verified with those from non-compact schemes. The results are also validated against experimental data. Finally, the flow around a pitching-plunging airfoil at low Reynolds number is simulated, as it is representative of the flow around a flapping-wing-based micro-air vehicle. Our results are compared with previous computational studies with second and third order spatial accuracy. Although lower order schemes are sufficient for accurate prediction of integrated forces, the higher order CRWENO scheme is able to resolve the small-scale flow structures near the airfoil surface, as well as the acoustic waves generated by the interaction of shed vortices with the airfoil.

Steady and unsteady flows around airfoils are simulated using the Jiang and Shu formulation of the WENO weights as well as a component-wise reconstruction of the flux vector in the present study. One of the drawbacks is the poor convergence of the CRWENO (and WENO) scheme for the steady, turbulent flow around an airfoil. Although the pressure distribution as well as the velocity profiles agreed with the experimental results, the residual dropped only an order of magnitude. The improvement of convergence of the CRWENO scheme with alternative formulations of the WENO weights is currently being investigated. The current formulation of the CRWENO scheme also causes oscillations in the higher derivatives of the solution, although the solution itself may be smooth and non-oscillatory. This is observed in the vortices shed from the pitching and plunging airfoil. Although the pressure and density distribution around the vortex is smooth, the numerical shadowgraph is oscillatory indicating lack of monotonicity in the second derivatives. These oscillations are sensitive to the smoothness indicators and the value of ϵ in the WENO weights and their alleviation is an area of active research.

Acknowledgments

References

[1] Hirsch C., "Numerical Computation of Internal and External Flows, Volume 1 & 2, Wiley Publishers, 1990.

[2] Laney C.B., "Computational Gasdynamics", Cambridge, UK: Cambridge University Press, 1998.

[3] Harten, A., Engquist, B., Osher, S., and Chakravarthy, S., "Uniformly high order essentially non oscillatory schemes, III", *Journal of Computational Physics*, Vol. 71, 1987, pp. 231–303.

[4] Shu, C.-W., and Osher, S., "Efficient implementation of essentially non-oscillatory schemes", *Journal of Computational Physics*, Vol. 77, 1988, pp. 439–471.

[5] Shu, C.-W., and Osher, S., "Efficient implementation of essentially non-oscillatory schemes, II", *Journal of Computational Physics*, Vol. 83, 1989, pp. 32–78.

[6] Liu, X., Osher, S., and Chan, T., "Weighted essentially non-oscillatory schemes", *Journal of Computational Physics*, Vol. 115, 1994, pp. 200–212.

[7] Jiang, G.-S., and Shu, C.-W., "Efficient implementation of weighted ENO schemes", *Journal of Computational Physics*, Vol. 126, 1996, pp. 202–228.

[8] Balsara, D.S., and Shu, C.-W., "Monotonicity preserving weighted essentially non-oscillatory schemes with increasingly high order of accuracy", *Journal of Computational Physics*, Vol. 160, 2000, pp. 405–452.

[9] Henrick, A.K., Aslam, T.D., and Powers, J.M., "Mapped weighted essentially non-oscillatory schemes: Achieving optimal order near critical points", *Journal of Computational Physics*, Vol. 207, 2005, pp. 542–567.

[10] Borges, R., Carmona, M., Costa, B., and Don, W.S., "An improved weighted essentially non-oscillatory scheme for hyperbolic conservation laws", *Journal of Computational Physics*, Vol. 227, 2008, pp. 3191–3211.

[11]Yamaleev, N.K., and Carpenter, M.H., "A systematic methodology for constructing high-order energy stable WENO schemes", *Journal of Computational Physics*, Vol. 228, 2009, pp. 4248–4272.

[12]Lele, S.K., "Compact finite difference schemes with spectral-like resolution", *Journal of Computational Physics*, Vol. 103, 1992, pp. 16–42.

[13]Pirozzoli, S., "Conservative hybrid compact-WENO schemes for shock-turbulence interaction", *Journal of Computational Physics*, Vol. 178, 2002, pp. 81–117.

[14]Ren, Y.-X., Liu, M., and Zhang, H., "A characteristic-wise hybrid compact-WENO scheme for solving hyperbolic conservation laws", *Journal of Computational Physics*, Vol. 192, 2003, pp. 365–386.

[15]Deng, X., and Maekawa, H., "Compact high-order accurate nonlinear schemes", *Journal of Computational Physics*, Vol. 130, 1997, pp. 77–91.

[16]Deng, X., and Zhang, H., "Developing high order weighted compact nonlinear schemes", *Journal of Computational Physics*, Vol. 165, 2000, pp. 22–44.

[17]Wang, S., and Huang, G.P., "An essentially nonoscillatory high order Padé-type (ENO-Padé) scheme", *Journal of Computational Physics*, Vol. 177, 2002, pp. 37–58.

[18]Ghosh, D., and Baeder, J.D., "Compact Reconstruction Schemes with Weighted ENO Limiting for Hyperbolic Conservation Laws", *SIAM Journal on Scientific Computing*, To Appear.

[19]Pulliam, T., "Time Accuracy and the use of Implicit Methods, *11th AIAA Computational Fluid Dynamics Conference*, AIAA Paper 1993-3360, Orlando, FL, July 1993.

[20]Jameson, A., and Yoon, S., "Lower-Upper Implicit Schemes with Multiple Grids for Euler Equations, *AIAA Journal*, Vol. 25, No. 7, 1987, pp. 929-935.

[21]Yoon, S., and Jameson, A., "Lower-Upper Symmetric-Gauss-Seidel Method for the Euler and Navier-stokes Equations, *AIAA Journal*, Vol. 26, No. 9, 1988, pp. 1025-1026.

[22]Warming, R., and Beam, R., "On the Construction and Application of Implicit Factored Schemes for Conservation Laws, *SIAM-AMS Proceedings*, Vol. 11, 1978, pp. 85-129.

[23]Pulliam, T., and Chaussee, D., "A Diagonal Form of an Implicit Approximate Factorization Algorithm, *Journal of Computational Physics*, Vol. 39, No. 2, 1981, pp. 347-363.

[24]Pandya, S. A., Venkateswaran, S., and Pulliam, T. H., "Implementation of Preconditioned Dual-Time Procedures in OVERFLOW, *41st AIAA Aerospace Sciences Meeting and Exhibit*, AIAA paper 2003-0072, Reno, NV, January 2003.

[25]Spalart, P.R., and Allmaras, S.R., "A One-Equation Turbulence Model for Aerodynamic Flows", AIAA Paper 92-0439, June 1992.

[26]Roe, P., "Approximate Riemann solvers, parameter vectors and difference schemes, *Journal of Computational Physics*, Vol. 135, No. 2, 1997, pp. 250–258.

[27]Lax, P.D., "Weak solutions of nonlinear hyperbolic equations and their numerical computation", *Communications on Pure and Applied Mathematics*, Vol. 7, 1954, pp. 159–193.

[28]Shu, C.-W., "Essentially Non-Oscillatory and Weighted Essentially Non-Oscillatory Schemes for Hyperbolic Conservation Laws", ICASE Report 97-65, 1997

[29]Zhang, S., Zhang, Y.-T., and Shu, C.-W., "Multistage interaction of a shock wave and a strong vortex", *Physics of Fluids*, Vol. 17, 2006, Paper 116101.

[30]Cook, P.H., McDonald, M.A., and Firmin, M.C.P., "Aerofoil RAE 2822 - Pressure Distributions, and Boundary Layer and Wake Measurements," Experimental Data Base for Computer Program Assessment, AGARD Report AR 138, 1979.

[31]Tatsumi, S., Martinelli, L., and Jameson, A., "A New High Resolution Scheme for Compressible Flows past Airfoil", AIAA Paper 95-0466, 1995

[32]Su, X., Sasaki D., and Nakahashi K., "Efficient implementation of WENO scheme on structured meshes", The 25th Computational Fluid Dynamics Symposium, Paper C01-3

[33]McAlister, K.W., Pucci, S.L., McCroskey, W.J., and Carr, L.W., "An Experimental Study of Dynamic Stall on Advanced Airfoil Sections", Vol. 2., NASA Technical Memorandum 84245, 1982.

[34]Yuan, W., Lee, R., Hoogkamp, E., and Khalid, M., "Numerical and Experimental Simulations of Flapping Wings", International Journal of Micro Air Vehicles, Vol. 2, No. 3, 2010, pp. 181–209.